

# Continuous Conversion of CT Kernel using Switchable CycleGAN with AdaIN

Serin Yang, Eung Yeop Kim, and Jong Chul Ye, *Fellow, IEEE*

**Abstract**—In X-ray computed tomography (CT) reconstruction, different filter kernels are used for different structures being emphasized. Since the raw sinogram data is usually removed after reconstruction, in case there are additional requirements for reconstructed images with other types of kernels that were not previously generated, the patient may need to be scanned again. Accordingly, there exists increasing demand for post-hoc image domain conversion from one kernel to another without sacrificing the image content. In this paper, we propose a novel unsupervised kernel conversion method using cycle-consistent generative adversarial network (cycleGAN) with adaptive instance normalization (AdaIN). In contrast to the existing deep learning approaches for kernel conversion, our method does not require paired dataset for training. In addition, our network can not only translate the images between two different kernels but also generate images on every interpolating path along an optimal transport between the two kernel image domains, enabling synergistic combination of the two filter kernels. Experimental results confirm the advantages of the proposed algorithm.

**Index Terms**—Computed tomography, reconstruction kernels, cycle-consistent adversarial networks, style transfer, adaptive instance normalization (AdaIN)

## I. INTRODUCTION

**I**N computed tomography (CT) images, raw sinogram data are collected from detectors, from which tomographic images are reconstructed using reconstruction algorithms such as filtered backprojection (FBP). Depending on the structural property of the object, researchers or clinicians should choose a specific reconstruction kernel and this selection affects the range of features that can be seen [1]. For example, high pass filters preserve higher spatial frequencies and decrease lower spatial frequencies, which introduces more noise. They are applicable to bone and tissues with high CT contrast. On the other hand, low pass filters preserve lower spatial frequencies and reduce higher spatial frequencies, which results in reduced noise but impairs spatial resolution. The filters are adequate for brain or soft tissue [1], [2].

Unfortunately, these routine reconstruction procedure introduces several limitations. First, different reconstructed datasets need to be created and stored in order to examine different structures being imaged. The size of the required storage can become quickly large to accommodate various types of kernel

images [3], [4]. Otherwise, radiologists can only see those previously saved images with fixed reconstruction kernel, as the raw sinogram data are usually removed after reconstructed images are generated. This means that in the event that reconstructed images with other types of kernels are needed that were not previously generated to identify new lesions or abnormalities that were never detected with the existing kernels, the patient would be referred again for additional scanning, causing additional cost and inconvenience.

One way to address this problem is a post-hoc kernel conversion. Specifically, CT images from one kernel are converted into those from another kernel using an image domain processing without performing additional reconstruction from the sinogram data. Unfortunately, this image domain filter kernel conversion is seen as a difficult task as the relationship between different kernel images needs to be found out and a new texture should be synthesized for the target domain.

Recently, a deep learning approach was explored for kernel conversion [5]. This approach is based on the supervised training, so that it can only be applied when there exists paired dataset from the different kernels. Although paired data sets for training could be generated from the same sinogram with different filter kernels, collecting all paired CT kernel image data sets for different CT scanners and acquisition conditions like KVp, mAs, etc. would be a daunting task that would only be done by careful planning of data acquisition for the future.

Therefore, one of the most important contributions of this work is an unsupervised deep learning approach that can be trained without paired data set. In particular, we consider the kernel conversion problem as an unsupervised image style transfer problem, and develop an unsupervised deep learning approach. In fact, cycle-consistent adversarial network (cycleGAN) [6] is one of the representative unsupervised image style transfer methods that can learn to translate between two different domains. Furthermore, our recent theoretical work [7] shows that the cycleGAN can be interpreted as an optimal transport [8], [9] by simultaneously minimizing the distances between the empirical data and synthesized data in two domains. Therefore, we use cycleGAN as our model, with each domain consisting of images that were reconstructed from two different kernels.

In contrast to the conventional cycleGAN that uses two distinct generators, another important contribution of our work is that our cycleGAN network is implemented using a single conditional generator with adaptive instance normalization (AdaIN) [10]. Accordingly, a single generator can be used for both forward and backward style transfer. In addition to reducing the memory requirement for the cycleGAN training

This work was supported by the National Research Foundation (NRF) of Korea grant NRF-2020R1A2B5B03001980.

S. Yang and J.C. Ye are with the Department of Bio and Brain Engineering, Korea Advanced Institute of Science and Technology (KAIST), Daejeon 34141, Republic of Korea (e-mail: yangsr, jong.ye@kaist.ac.kr). E.Y. Kim is with the Department of Radiology, Gil Medical Center, Gachon University College of Medicine, Incheon, Republic of Korea (e-mail: neurorad-kim@gmail.com)

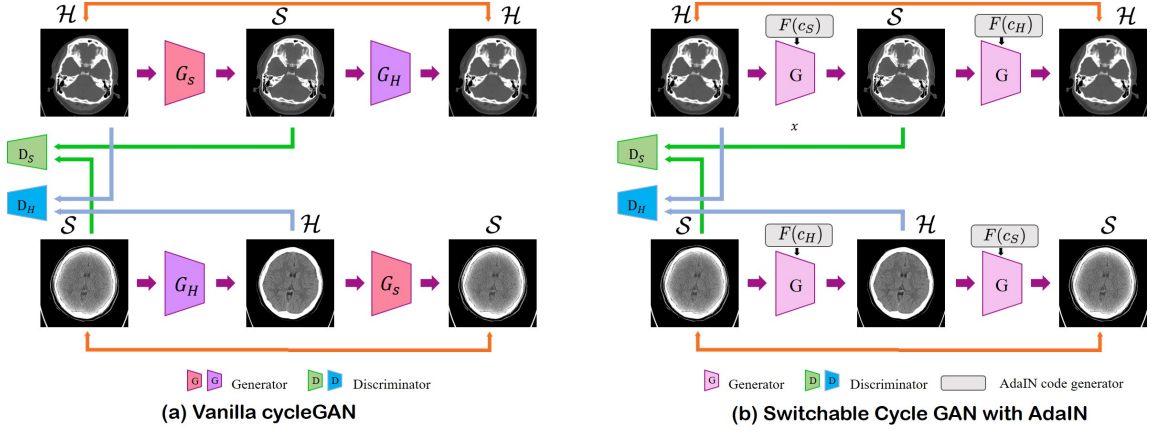


Fig. 1: Vanilla cycleGAN and our switchable cycleGAN with AdaIN layers for H and S kernel conversion.

[11], the proposed conditional generator with AdaIN layer can generate every interpolating path along an optimal transport path between two target domains at the inference phase, which brings us an opportunity to discover new objects or tissues which could not have been observed with the currently given two reconstruction kernels.

This paper is organized as follows. CT conversion and image style transfers are first reviewed in Section II, after which we explain how these techniques can be synergistically combined for our kernel conversion algorithm in Section III. Section IV describes the data set and experimental setup. Experimental results are provided in Section V, which is followed by Conclusions in Section VII.

## II. RELATED WORKS

### A. CT Kernel Conversion

In classical approaches for CT kernel conversion, one common way is to combine two different kernel images into one for better diagnostic purpose [3], [4], [12]. Unfortunately, the optimality of the combined filter kernel is a subjective matter, which depends on the clinical applications. In this regard, deep learning approaches for CT kernel conversion [5], [13] do not interfere with the existing clinical workflows, as the generated images are still in the standard kernel sets. Furthermore, a radiomic study revealed that the generated images do not sacrifice the accuracy of the diagnosis [13]. However, this method does not generate new kind of hybrid informations that could be obtained in the aforementioned kernel combination methods.

### B. Deep Learning for Image Style Transfer

There are currently two types of approaches for image style transfer. First, a content image and a style reference image are given to a neural network, and the goal is to convert the content image to have styles from the style reference. For example, Gatys et al. [14] solves an optimization problem in the feature spaces between the content and style images. However, the iterative optimization processes take significant time and the results are easily overly stylized. Instead, the adaptive instance normalization (AdaIN) was proposed as a

simple alternative [10]. Specifically, AdaIN layer estimates the means and variances of referenced style features and uses them to correct bias and scaling factors. Despite the simplicity, a recent theoretical works [15] showed that the style transfer by AdaIN is a special case of optimal transport [8], [9] between two image distributions.

Another type of style transfer is performed as a distribution matching approach. For example, converting spring scenes to the winter scene corresponds to this approach. Specifically, let the target style images lie in the domain  $\mathcal{X}$  equipped with a probability measure  $\mu$ , whereas the input content images lie in  $\mathcal{Y}$  with a probability measure  $\nu$ . Then, the image style transfer is to transport the content distribution  $\nu$  to the style image distribution  $\mu$ , and vice versa. In our recent theoretical work [7], we show that this type of style transfer problem can be solved through optimal transport [8], [9]. In particular, if we define the transportation cost as the sum of the statistical distances between the empirical distribution and the generated distribution in  $\mathcal{X}$  and  $\mathcal{Y}$ , respectively, and try to find the joint distribution that minimizes the sum of the distances, then the Kantorovich dual formulation [8], [9] leads to the cycleGAN formulation. This justifies why cycleGAN has become a representative style transfer method.

By synergistically combining the two ideas, we recently proposed switchable cycleGAN [11] that combines AdaIN into cycleGAN so that only a single generator can be used for style transfer between two domains. Although the original motivation of [11] was to reduce the memory requirement for the cycleGAN training by eliminating additional adddiscriminators, in the following we will show that a similar cycleGAN with AdaIN not only reduces the memory but also generates every interpolating points along an optimal transport path between two domains, leading to diverse kernel conversions.

## III. THEORY

### A. Switchable cycleGAN for Kernel Conversion

Specifically, let the domain  $\mathcal{S}$  be composed of CT images from soft tissue kernel (S kernel), whereas the images in the domain  $\mathcal{H}$  are generated by bone kernel (H kernel). Then, as shown in Fig. 1(a), a standard cycleGAN framework for

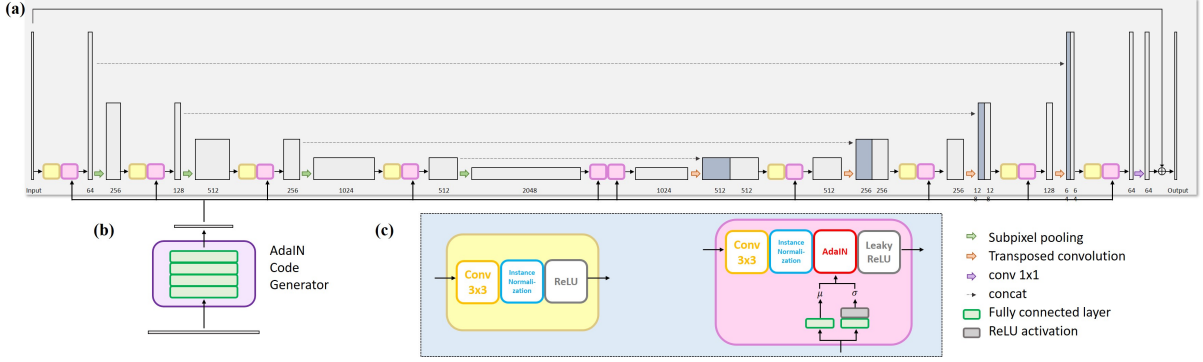


Fig. 2: (a) Generator architecture using polyphase pooling and AdaIN layers. (b) AdaIN code generator architecture. (c) Detailed diagram of key blocks in our generator.

kernel conversion would require two generators: the forward generator from H kernel to S kernel ( $G_S$ ), the backward generator from S kernel to H kernel images ( $G_H$ ).

In contrast, our switchable cycleGAN implements two generators using a single baseline autoencoder network  $G$  followed by AdaIN-based optimal transport layers. More specifically, to generate images in  $\mathcal{H}$  domain, we use an autoencoder as the baseline network and then use the AdaIN transform to transport the autoencoder features to the H kernel features. Similarly, for  $\mathcal{S}$  domain image generation, the autoencoder features are also transported to the S-kernel features using another AdaIN transform.

More specifically, let a multi-channel autoencoder feature map at a specific layer be represented by

$$\mathbf{x} = [\mathbf{x}_1 \quad \cdots \quad \mathbf{x}_P] \in \mathbb{R}^{HW \times P}, \quad (1)$$

where  $\mathbf{x}_i \in \mathbb{R}^{HW \times 1}$  refers to the  $i$ -th column vector of  $\mathbf{x}$ , which represents the vectorized feature map of size of  $H \times W$  at the  $i$ -th channel. Then, AdaIN changes the feature data for each channel using the following transform:

$$\mathbf{z}_i = \mathcal{T}(\mathbf{x}_i, \mathbf{y}_i), \quad i = 1, \dots, P \quad (2)$$

where

$$\mathcal{T}(\mathbf{x}, \mathbf{y}) := \frac{\sigma(\mathbf{y})}{\sigma(\mathbf{x})} (\mathbf{x} - m(\mathbf{x})\mathbf{1}) + m(\mathbf{y})\mathbf{1}, \quad (3)$$

where  $\mathbf{1} \in \mathbb{R}^{HW}$  is the  $HW$ -dimensional vector composed of 1, and  $m(\mathbf{x})$  and  $\sigma(\mathbf{x})$  are the mean and standard deviation (std) for  $\mathbf{x} \in \mathbb{R}^{HW}$ .

In (3), target domain mean  $m(\mathbf{y})$  and std  $\sigma(\mathbf{y})$  are often called AdaIN vectors, which are usually adaptively learned from the data. Specifically, a key idea of our switchable cycleGAN with AdaIN layer is to use different  $\sigma(\mathbf{y})$  and  $m(\mathbf{y})$  vectors for the forward and backward generators, respectively. More specifically, the architecture of the proposed generator network is shown in Fig. 2. Basic structure of the autoencoder network is from U-Net [16], where the pooling layer is replaced with lossless polyphase decomposition [17], which will be explained later. In our autoencoder, the batch normalization layers are replaced with AdaIN layers, which take output AdaIN code  $(m(\mathbf{y}), \sigma(\mathbf{y}))$  from the AdaIN code generator  $F(c)$ , where  $c$  denotes the target domain code.

## B. Cycle-Consistent Adversarial Training

Fig. 1(b) visualizes the learning scheme of the proposed method, which can be represented by an min-max optimization problem:

$$\min_{G, F} \max_{D_H, D_S} \ell_{total}(G, F, D_S, D_H) \quad (4)$$

where the total loss is given by

$$\begin{aligned} \ell_{total}(G, F, D_S, D_H) = & -\ell_{disc}(G, F, D_S, D_H) + \\ & \lambda_{cyc} \ell_{cycle}(G, F) + \\ & \lambda_{id} \ell_{identity}(G, F) \end{aligned} \quad (5)$$

where  $\lambda_{cyc}$  and  $\lambda_{id}$  denote the weighting parameters for the cycle loss and the identity loss terms. We use  $\lambda_{cyc} = 10$  and  $\lambda_{id} = 5$  for our experiments.

Here, the discriminator loss  $\ell_{disc}(G, F, D_S, D_H)$  is composed of LSGAN losses [18]:

$$\begin{aligned} \ell_{disc}(G, F, D_S, D_H) = & \mathbb{E}_{y \sim P_{\mathcal{H}}} \left[ \frac{1}{N} \|D_H(y)\|_2^2 \right] + \mathbb{E}_{x \sim P_{\mathcal{S}}} \left[ \frac{1}{N} \|1 - D_H(G(x; F(c_H)))\|_2^2 \right] \\ & + \mathbb{E}_{x \sim P_{\mathcal{S}}} \left[ \frac{1}{N} \|D_S(x)\|_2^2 \right] + \mathbb{E}_{y \sim P_{\mathcal{H}}} \left[ \frac{1}{N} \|1 - D_S(G(y; F(c_S)))\|_2^2 \right] \end{aligned}$$

where  $\|\cdot\|_2$  is the  $l_2$  norm,  $N$  denotes size of input  $x$  or  $y$ , and  $D_S$  (resp.  $D_H$ ) is the discriminator that tells the fake S kernel (resp. H kernel) images from real S kernel (resp. H kernel) images, and  $c_H$  and  $c_S$  denotes the target codes indicating H and S kernel domains, respectively. The cycle loss  $\ell_{cyc}(G, F)$  in (5) is defined as:

$$\begin{aligned} \ell_{cyc}(G, F) = & \mathbb{E}_{y \sim P_{\mathcal{H}}} [\|G(G(y; F(c_S)); F(c_H)) - y\|_1] \\ & + \mathbb{E}_{x \sim P_{\mathcal{S}}} [\|G(G(x; F(c_H)); F(c_S)) - x\|_1] \end{aligned} \quad (6)$$

In addition, the identity loss in (5) is given by

$$\begin{aligned} \ell_{id}(G, F) = & \mathbb{E}_{y \sim P_{\mathcal{H}}} [\|G(y; F(c_H)) - y\|_1] \\ & + \mathbb{E}_{x \sim P_{\mathcal{S}}} [\|G(x; F(c_S)) - x\|_1] \end{aligned} \quad (7)$$

The training of AdaIN code generator  $F(c)$  is to provide the following output:

$$F(c) = \begin{cases} (\sigma(\mathbf{x}), m(\mathbf{x})), & c = c_H \\ (\sigma(\mathbf{y}), m(\mathbf{y})), & c = c_S \end{cases} \quad (8)$$

Here,  $(\sigma(\mathbf{y}), m(\mathbf{y}))$  are learnable vectors, whereas  $(\sigma(\mathbf{x}), m(\mathbf{x}))$  are calculated at the inference phase from each feature layers. Then, this leads to the following AdaIN transform:

$$\mathcal{T}(\mathbf{x}, \mathbf{y}; c) = \begin{cases} \mathbf{x}, & c = c_H \\ \frac{\sigma(\mathbf{y})}{\sigma(\mathbf{x})}(\mathbf{x} - m(\mathbf{x})\mathbf{1}) + m(\mathbf{y})\mathbf{1}, & c = c_S \end{cases} \quad (9)$$

This implies that for the generation of  $\mathcal{S}$  domain images, the AdaIN layers take the learned output vectors from the AdaIN code generator, whereas this step is not necessary for the generation of  $\mathcal{H}$  domain images.

### C. Kernel Synthesis along an Optimal Transport Path

There are several advantages of using our switchable cycleGAN. First, the neural network for the AdaIN code generator is very light, whose network complexity is negligible compared to additional generator in the conventional cycleGAN. Accordingly, the network weights can be significantly reduced, which makes the algorithm trained more robust even with small number of training data set.

Yet another important advantage of our method is the continuous synthesis of kernels at the inference time. In order to understand this claim, we need to revisit the link of AdaIN to optimal transport [8], [9]. Specifically, let the two probability spaces  $\mathcal{U} \subset \mathbb{R}^{HW}$  and  $\mathcal{V} \subset \mathbb{R}^{HW}$  be equipped with the Gaussian probability measure  $\mu \sim \mathcal{N}(\mathbf{m}_U, \Sigma_U)$  and  $\nu \sim \mathcal{N}(\mathbf{m}_V, \Sigma_V)$ , respectively, where  $\mathbf{m}_U$  and  $\Sigma_U$  denote the mean vector and the covariance matrix, respectively. Then, a closed form optimal transport map from the measure  $\mu$  to the measure  $\nu$  with respect to Wasserstein-2 distance can be obtained [15]. In particular, if we assume i.i.d. distribution, i.e.

$$\mathbf{m}_U = m(\mathbf{x})\mathbf{1}, \Sigma_U = \sigma(\mathbf{x})\mathbf{I}, \mathbf{m}_V = m(\mathbf{y}), \Sigma_V = \sigma(\mathbf{y})\mathbf{I}$$

where  $\mathbf{I}$  is the identity matrix, then the authors in [15] showed that the optimal transport map between the two probability measures is given by

$$T_{\mu \rightarrow \nu}(\mathbf{x}) = m(\mathbf{y})\mathbf{1} + \frac{\sigma(\mathbf{y})}{\sigma(\mathbf{x})}(\mathbf{x} - m(\mathbf{x})\mathbf{1}) \quad (10)$$

which is equivalent to the AdaIN transform in (3).

Given that our AdaIN codes for generating  $\mathcal{H}$  and  $\mathcal{S}$  domains are  $(m(\mathbf{x}), \sigma(\mathbf{x}))$  and  $(m(\mathbf{y}), \sigma(\mathbf{y}))$ , respectively, we can consider the intermediate distribution with interpolated mean and variances:

$$m(\alpha; \mathbf{x}, \mathbf{y}) = (1 - \alpha)m(\mathbf{x}) + \alpha m(\mathbf{y}) \quad (11)$$

$$\sigma(\beta; \mathbf{x}, \mathbf{y}) = (1 - \beta)\sigma(\mathbf{x}) + \beta\sigma(\mathbf{y}) \quad (12)$$

for  $0 \leq \alpha, \beta \leq 1$ . Then, the optimal transport from the i.i.d. Gaussian distribution  $\mu \sim \mathcal{N}(m(\mathbf{x})\mathbf{1}, \sigma(\mathbf{x})\mathbf{I})$  to another i.i.d. Gaussian distribution  $\eta \sim \mathcal{N}(m(\alpha)\mathbf{1}, \sigma(\beta)\mathbf{I})$  is given by

$$\begin{aligned} T_{\mu \rightarrow \eta}(\mathbf{x}) &= m(\alpha; \mathbf{x}, \mathbf{y})\mathbf{1} + \frac{\sigma(\beta; \mathbf{x}, \mathbf{y})}{\sigma(\mathbf{x})}(\mathbf{x} - m(\mathbf{x})\mathbf{1}) \\ &= (1 - \beta)\mathbf{x} + \beta \left( m(\mathbf{y})\mathbf{1} + \frac{\sigma(\mathbf{y})}{\sigma(\mathbf{x})}(\mathbf{x} - m(\mathbf{x})\mathbf{1}) \right) \\ &\quad + (\beta - \alpha)(m(\mathbf{x}) - m(\mathbf{y})) \end{aligned}$$

From this transport plan, we can see that if the means of the feature maps are similar, i.e.  $m(\mathbf{x}) \simeq m(\mathbf{y})$ , then the AdaIN transform is mainly changed by  $\beta$  parameters. In this case, the optimal transport path is similar to a path with  $\alpha = \beta$ , which can be further simplified as

$$T_{\mu \rightarrow \eta}(\mathbf{x}) = (1 - \alpha)\mathbf{x} + \alpha \left( m(\mathbf{y})\mathbf{1} + \frac{\sigma(\mathbf{y})}{\sigma(\mathbf{x})}(\mathbf{x} - m(\mathbf{x})\mathbf{1}) \right)$$

where  $\alpha$  ranges from zero to one. Therefore, once training is done, continuous kernel image synthesis can be possible at the inference phase by simply changing  $\alpha$ .

## IV. METHODS

### A. Data Acquisition

To verify the proposed continuous kernel conversion, we use the following dataset provided from Gachon University Gil Hospital.

1) *Head dataset*: Head images from 11 patients were obtained (SOMATOM Definition Edge, Siemens Healthineers, Germany). Each patient had two sets of images, each of which was generated with H and S kernels, respectively. Each patient data consisted of around 50 slices. Accordingly, total 540 slices were achieved. One patient was excluded because of its different image matrix size ( $571 \times 512$  vs.  $512 \times 512$ ). We used seven patients for training, two for validation, the other one patient for test (44 slices). Totally, we used ten patients consisting of three men and seven women with mean age  $39.7 \pm 19.143$  years.

2) *Facial bone dataset*: Facial bone images of 12 patients were obtained. Similar to the head dataset, each patient data was composed of reconstructed images with H and S kernels for bone and brain, respectively. Each patient data involved different number of slices from 48 to 189 slices, producing 1683 slices of facial bone images for each kernel. One patient was excluded because of its different image matrix size ( $512 \times 534$  vs.  $512 \times 512$ ). We used eight patients for training, two for validation, the remaining one patient for test (165 slices). Totally, we used 11 patients consisting of four men and seven women with mean age  $32.3 \pm 15.435$  years.

3) *Hypopharyngeal cancer dataset*: The dataset involves CT images of one patient suffering from hypopharyngeal cancer, which leads to the demand for cartilage abnormality detection. The images covered from head to chest of its patient. The single volume was comprised of 110 slices. We used a half of the slices for fine-tuning the model after training, and the other half for inference.

### B. Kernels

For head dataset, J30s and J70h kernels were used. For facial bone dataset, J40s and J70h kernels were applied to reconstruct CT images. J30s and J40s kernels are low pass filters which are adequate for soft tissue. J70h kernel is a representative of high pass filters and usually used to observe bone. In this paper, we refer to J30s and J40s kernels as S kernel and J70h kernel as H kernel. Different from the two dataset, hypopharyngeal cancer images were reconstructed with Br44 kernel, which has similar property as S kernel.

### C. Network Architecture

1) *Autoencoder*: The autoencoder used in this paper is based on the U-Net architecture with pooling layer implemented by polyphase decomposition [17]. It has skip connections between encoder and decoder parts, which enable inputs and outputs to share information. Also, the input is added pixel-wise to the output at the end of the network. The network, therefore, learns residuals. In conventional encoder-decoder networks, the input images go through several down-sampling layers until a bottleneck layer, in order for a network to extract low frequency information. Through the down-sampling layers, the network necessarily loses significant amount of information which plays a crucial role in auto-encoder learning. Therefore, instead of using pooling layers, we used all the given information which can be achieved by lossless decomposition using polyphase decomposition as shown in Fig. 3(a). Specifically, at the layers where a pooling operation is required, we arranged all the pixels into four groups. It can be thought as having a  $2 \times 2$  filter with stride of 2 in order not to make overlapping. The first pixels of each sub-region gather together to form new output. Also, the second pixels assemble another output. In the same manner, the third and fourth pixels make the third and fourth outputs, respectively. These four outputs are stacked along a channel direction. After this sub-pixel pooling operation, the size of final output would be reduced by half while the number of channels would increase fourfold.

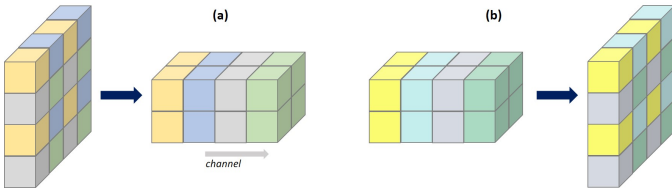


Fig. 3: (a) Pooling layer using polyphase decomposition process. Pixels are divided into four groups and each group composes one image of a reduced size. Then, the groups are stacked along channel direction. (b) Unpooling layer using polyphase recomposition.

Unpooling operation using polyphase recomposition can be done in exactly the opposite way of polyphase pooling operation as shown in Figure 3(b). Interestingly, unpooling operation in a decoder part can be extended to a transposed convolution. Transposed convolution involves both polyphase recomposition and filtering operation. While polyphase unpooling requires fixed position for each pixel, transposed

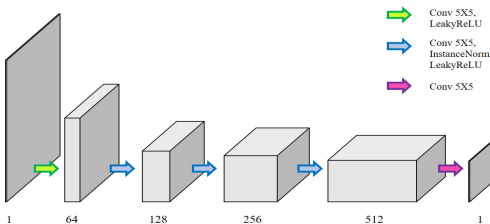


Fig. 4: Architecture of the discriminator.

convolution does not have any positional condition to follow. When using transposed convolution, the network parameters are, therefore, chosen to be optimal without any specific restriction. This results in experimentally better performance of the network with transposed convolution compared to unpooling operation using polyphase recomposition. Thus, we used transposed convolution in our proposed Polyphase U-Net.

2) *Discriminator*: We used as a discriminator PatchGAN [19] which shows good performance at capturing high frequency information because it focuses only on the scale of its patches, not the entire image. The illustration of the discriminator is shown in Figure 4. The input whose size is  $128 \times 128$  with one channel passes through a convolution layer with stride two. Then, next convolution layer with stride two gets the feature map of size  $62 \times 62$ . The feature maps go through two successive convolution layers with stride one. Finally, the output is convolved with the last convolution layer. Kernel size of all the convolution layers in the discriminator is  $5 \times 5$ . Final output size is  $24 \times 24$  which was chosen empirically.

3) *AdaIN Code Generator*: Details about the architecture of AdaIN code generator are illustrated in Figure 2. One vector of size 128 is input to shared code generator. The shared code generator includes four fully connected layers with output size of 64. The final output code is given to 10 convolution blocks in the generator of cycleGAN. Since these convolution blocks have different number of channels, mean and variance code vectors are generated separately for each convolution block. For mean code vector, one fully connected layer is applied. ReLU activation layer is applied in addition to one fully connected layer for variance code vector because of non-negative property of variance.

### D. Training detail

The input images were randomly cropped into small patches of size  $128 \times 128$  during training. They were also randomly flipped both horizontally and vertically. Despite small size of dataset, patch-based training with random flipping provided an effect of data augmentation and enabled more stable training [20]. The learning rate was set as  $10^{-4}$  and  $10^{-5}$  for Head and Facial bone dataset, respectively. The Adam optimization algorithm [21] was used with batch size 8 and 16 for Head and Facial bone dataset, respectively, and the momentum parameters  $\beta_1 = 0.9, \beta_2 = 0.999$ . We saved models with the best quantitative results with validation data set and tested the models using 5-fold cross validation scheme. We implemented the networks using PyTorch library [22]. We trained the networks using two NVIDIA GeForce GTX 2080 Ti.

### E. Comparative studies

First, we compared our algorithm with classical kernel conversion approaches. Classical methods considered kernel conversion as kernel smoothing and sharpening. Specifically, to convert H kernel images into S kernel ones, frequency band decomposition and alteration of energy in each band were performed [23]. For the conversion from S to He kernel, we sharpened the S kernel images using Laplacian filter kernel

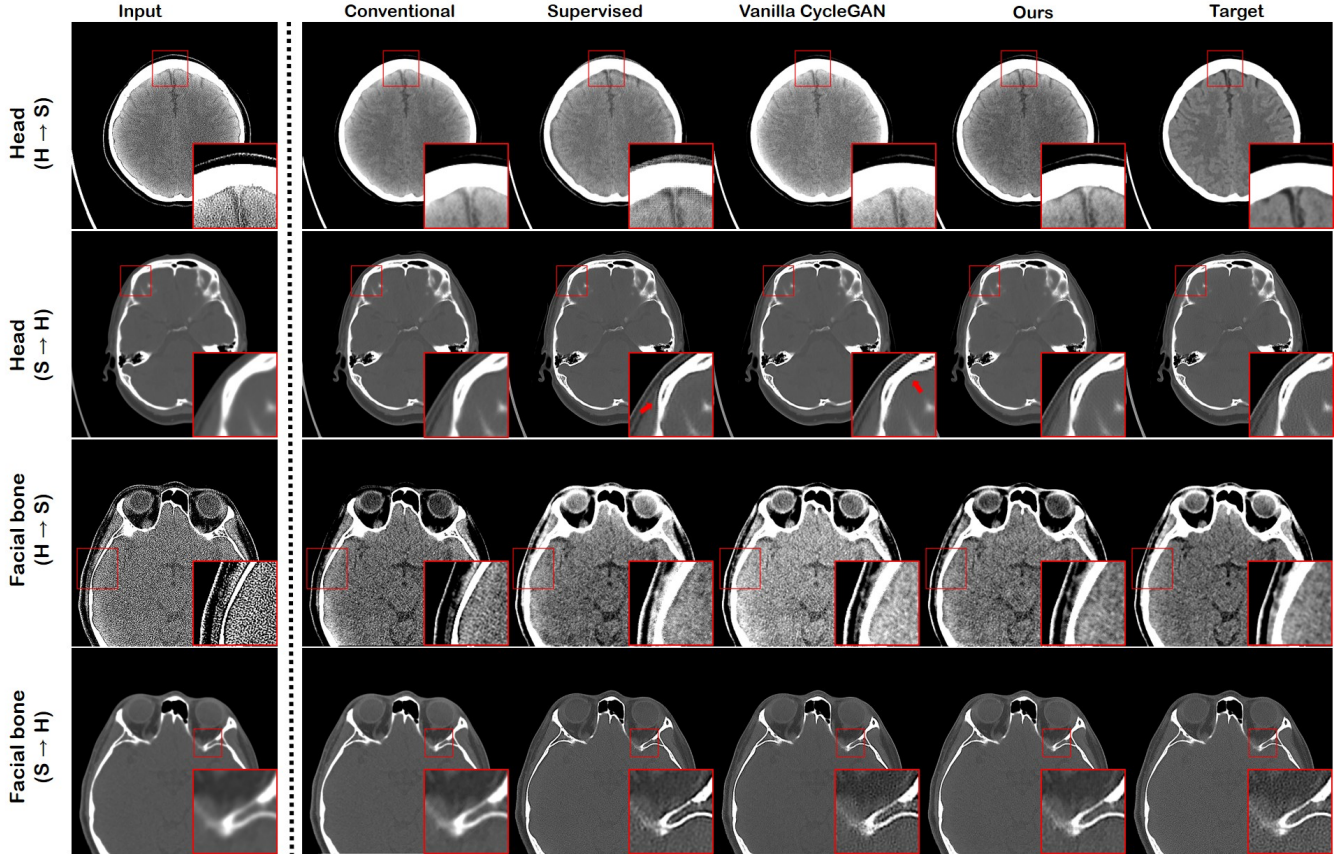


Fig. 5: Kernel conversion results by the classical method, supervised learning, vanilla cycleGAN, and the proposed switchable cycleGAN with AadIN. The first two rows are from Head dataset and the last two rows are from Facial bone dataset.

and Wiener-Hunt deconvolution method with estimated point spread function [24].

Moreover, we compared our proposed model with supervised learning method. For supervised learning method, the same generator architecture as our method was used as networks [17] and the mean squared error loss between output and ground truth images was used. Two different networks were trained separately for two opposite directional kernel translation. Batch size was 8 and 32 for Head and Facial bone dataset, respectively. Other settings for training were same as the proposed model.

In addition to the supervised learning method, we conducted comparative studies using vanilla cycleGAN [6]. Again, same U-Net architecture with polyphase decomposition was used for two generators. Due to the need to train two distinct generators, the total number of trainable weights increased compared to our method (see Figure 1). Batch size was 8 and 40 for Head and Facial bone dataset, respectively. The other training details were applied same as the proposed model.

#### F. Evaluation metrics

Since ground-truth data are available for the two types of dataset, we used peak signal to noise ratio (PSNR) as our quantitative metric, which is defined as follows:

$$PSNR = 10 \log_{10} \left( \frac{MAX_x^2}{MSE} \right) \quad (13)$$

$$MSE = \frac{1}{N_1 N_2} \sum_{i=0}^{N_1-1} \sum_{j=0}^{N_2-1} [x_{i,j} - \hat{x}_{i,j}]^2 \quad (14)$$

where  $N_1$  and  $N_2$  are row and column dimensions of the images,  $x_{i,j}$  denotes the  $(i,j)$ -th pixel, and  $MAX_x$  is the maximum possible pixel value of image  $x$ . We also used structural similarity (SSIM) index [25] which is defined as

$$SSIM(x, \hat{x}) = \frac{(2m_x m_{\hat{x}} + c_1)(2\sigma_{x\hat{x}} + c_2)}{(m_x^2 + m_{\hat{x}}^2 + c_1)(\sigma_x^2 + \sigma_{\hat{x}}^2 + c_2)} \quad (15)$$

where  $m$  is average of the image,  $\sigma$  is variance of the image, and  $\sigma_{x\hat{x}}$  is covariance of the images  $x$  and  $\hat{x}$ . The two variables  $c_1 = (k_1 L)^2$  and  $c_2 = (k_2 L)^2$  are used to stabilize the division where  $L$  is the dynamic range of the pixel intensities and  $k_1 = 0.01, k_2 = 0.03$  by default.

## V. EXPERIMENTAL RESULTS

### A. Comparison with previous methods

First, we compared our proposed model with classical kernel conversion method, supervised learning method, and vanilla cycleGAN [6]. In Figure 5 and Table I, the images generated from the classical method showed the worst performance in both quantitative and qualitative perspectives. Although higher PSNR and SSIM values were obtained for supervised learning

TABLE I: Quantitative comparison of various methods

Head	PSNR		SSIM	
	H	S	H	S
Classical method	12.4335	14.4620	0.6633	0.7401
Supervised (MSE Loss)	32.6624	24.2981	0.9022	0.8336
Vanilla CycleGAN	30.8758	21.9194	0.8913	0.8161
CycleGAN with AdaIN	31.6671	23.9193	0.8922	0.87664

Facial Bone	PSNR		SSIM	
	H	S	H	S
Classical method	13.1227	10.4685	0.5198	0.5369
Supervised (MSE Loss)	28.3261	21.1531	0.8079	0.8088
Vanilla CycleGAN	25.5337	17.4077	0.7135	0.7966
CycleGAN with AdaIN	26.6328	19.5712	0.7563	0.8336

in Table I, the qualitative results showed some blurring effect as shown in Figure 5, where the results were better with our method. More details are as follows:

1) *S kernel from H kernel*: Image translation from H kernel images to S kernel images is shown in the first and third rows of Figure 5. For S kernel images, soft tissue, such as blood vessels, should be clearly detected rather than bones. It is shown that performance of the our proposed method is apparently better than the supervised and vanilla cycleGAN methods. As can be seen in the first row of Fig. 5, the irrelevant patterns appeared on the result of the supervised model. The images generated from cycleGAN could not follow data distribution and pixel intensities around bone were significantly elevated. However, those artifacts were not shown in the results of our method. We believe that the artifacts for the supervised learning and vanilla cycleGAN may occur due to the limited training data set, but for the given training data set, we found that our proposed model has its strength in capturing the data distribution much more effectively.

Also, the third row of Fig. 5 demonstrates that bone shapes from conventional method were apparently different from the target images. Moreover, much more noise were involved in the results of the conventional method and the supervised learning model with respect to those of the other two unsupervised learning methods. S kernel images should clearly show soft tissues which require noise reduction. This can be easily seen from input and target images. In this point of view, our proposed model was better at translating H kernel images into S kernel ones than the supervised or vanilla cycleGAN.

2) *H kernel from S kernel*: H kernel images are usually used to gather information about clear outlines of bone. The images generated from S kernel images should contain information about clear delineation of bone. Results of image translation from S kernel images to H kernel images are shown in the second and fourth rows of Figure 5. The conventional method sharpened the input S kernel images but their sharpness was far below that of the target ones. Meanwhile, the results of all three deep-learning methods were similar. They could not only generate sharp bone outlines from blurred S kernel images, but also follow texture of H kernel domain. However, some artifacts occurred along bones in the supervised and cycleGAN methods (Figure. 5).

3) *Contributing factors of AdaIN to improved quality*: The model in one direction, from S kernel to H kernel, is actually

same as vanilla cycleGAN since it utilizes mean and variance of its own instead of those estimated from AdaIN. Thus, the H kernel images generated from our model showed almost equivalent quality to those from vanilla cycleGAN both in qualitative and quantitative results (Table I,  $p > 0.05$  for  $t$ -test on SSIM of generated H images on Head dataset). On the other hand, the model in the other direction, which translates H kernel images into S kernel ones, involves AdaIN so that mean and variance of H kernel domain are scaled and added, respectively. It can be noted that image quality of our proposed model enhanced a lot with respect to that of vanilla cycleGAN. It is supported in both qualitative and quantitative results. The artifacts could be observed in generated S kernel images from vanilla cycleGAN method and this made it difficult to accurately distinguish boundaries between bone and soft tissue. In addition, pixel intensities around bone were raised in the images from vanilla cycleGAN. However, these artifacts disappeared in the generated S kernel images from our model (Figure 5). Also, evaluation metrics significantly improved in case of generating S kernel images (Table I,  $p < 0.01$  for  $t$ -test on PSNR of generated S images on both Head and Facial bone dataset and SSIM of generated S images on Head dataset). The effectiveness of AdaIN was clearly shown through this different increase in image quality between two opposite directions.

Recall that the small dataset can be a leading factor to network overfitting. However, thanks to AdaIN, the number of model parameters reduced in half and the model learning has been shown to be more stable [11].

### B. Interpolation between two kernel images

During the training phase, we fixed  $\alpha$  as one in case of generating S kernel images and as zero in case of generating H kernel ones, so that AdaIN was applied only when translating images from H to S kernel. Once the training was done, at the inference phase different  $\alpha$  values were applied to generate interpolating kernel images along an optimal transport path. Thus, it did not affect any of training steps.

Since any arbitrary values can be chosen as  $\alpha$ , we could create combined kernel images along the interpolation path along the optimal transport trajectory (Fig. 6 and 7). The process of noise reduction was observed in the case of interpolation from zero to one, which is for generating S kernel images. Furthermore, we could see objects which were not able to be observed through previous kernels.

In particular, once our proposed method is applied, cartilage abnormality can be detected even with CT images as shown in Figure 8. For hypopharyngeal cancer case, it is important to check whether thyroid cartilage is invaded or not. This identification usually relies on magnetic resonance imaging since it is hard to observe the abnormality from CT images. However, with the help of our proposed method, discontinuity in outer border of cartilage could be discovered from the generated images. In addition, for  $\alpha = 0$ , overshoots and undershoots occurred in order to highlight the outlines of bone, which hindered close observation on bone shapes. However, more accurate examination could become possible by adjusting  $\alpha$  values to be larger than zero. Specifically, the images

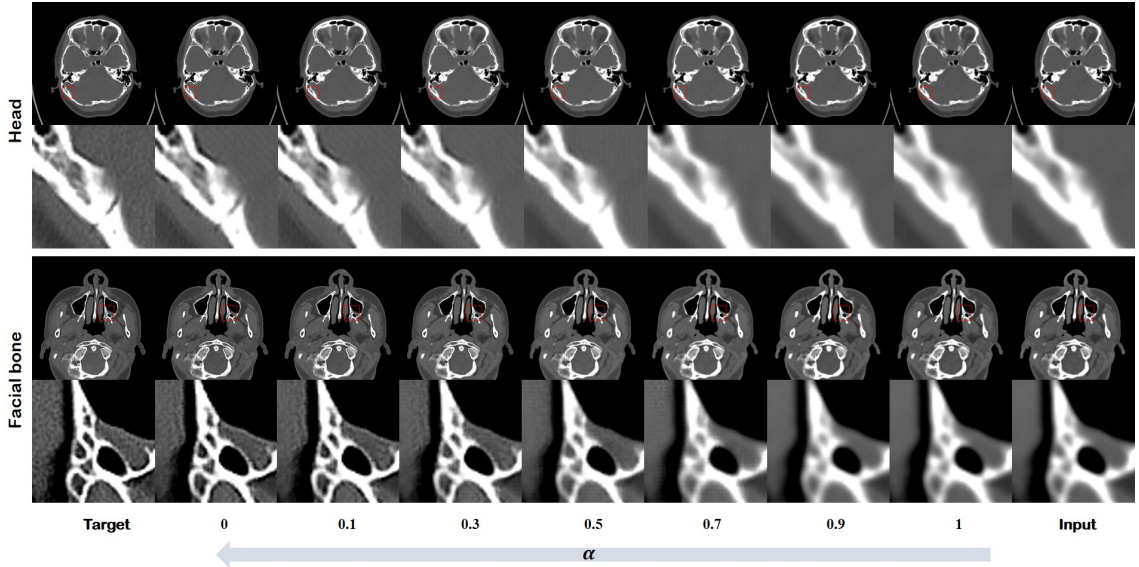


Fig. 6: Continuous interpolation of kernel images along an optimal transport path.

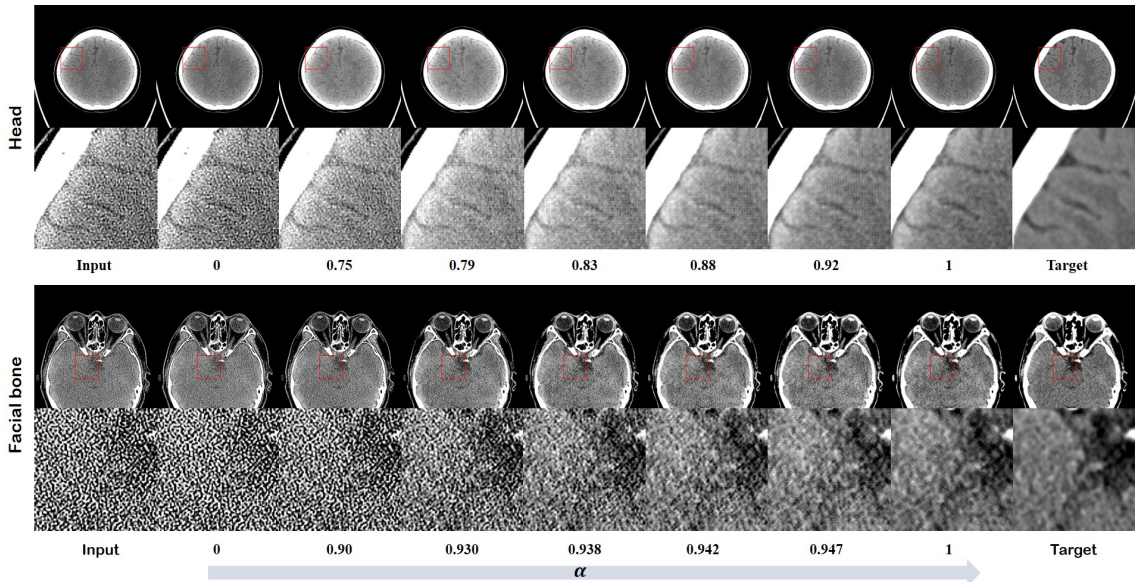


Fig. 7: Continuous interpolation of kernel images along an optimal transport path.

from  $\alpha$  larger than zero could be generated with smoother texture compared to those from  $\alpha = 0$ . This resulted in clear delineation with no more undershoot or overshoot around the bone but maintaining its shape as shown Figure 8. This example clearly shows the clinical usage of the continuous conversion of the filter kernels along the optimal transport path. Although it is easy to guess, it is reminded that the simple image domain weighted sum does not provide such synergistic information as ours since it is a simple mixing of image domain textures.

## VI. DISCUSSION

### A. Effect of Polyphase U-Net

Here, we investigated the differences between U-Net and Polyphase U-Net as a generator in our switchable cycleGAN.

For fair comparison with original U-Net [16], we reduced the number of channels in the generator. The total number of parameters in the Polyphase U-Net is around 30 millions. As shown in Figure 9, Polyphase U-Net showed enhanced performance compared to the U-Net [16]. Since S kernel images were blurry, we could not figure out the exact shape of bones with the S kernel images. However, the images generated from the Polyphase U-Net were highly similar to the target images reconstructed with H kernel regarding not only outlines of bones but also textures. The shapes of bones well followed the target images and they were clear enough to identify the small structures. Moreover, a broken nasal bone has been difficult to detect with the image reconstructed with S kernel (Figure 9, third row). The existence of the bone could only be confirmed. However, it has been well depicted in the image reconstructed from H kernel. This feature should be well

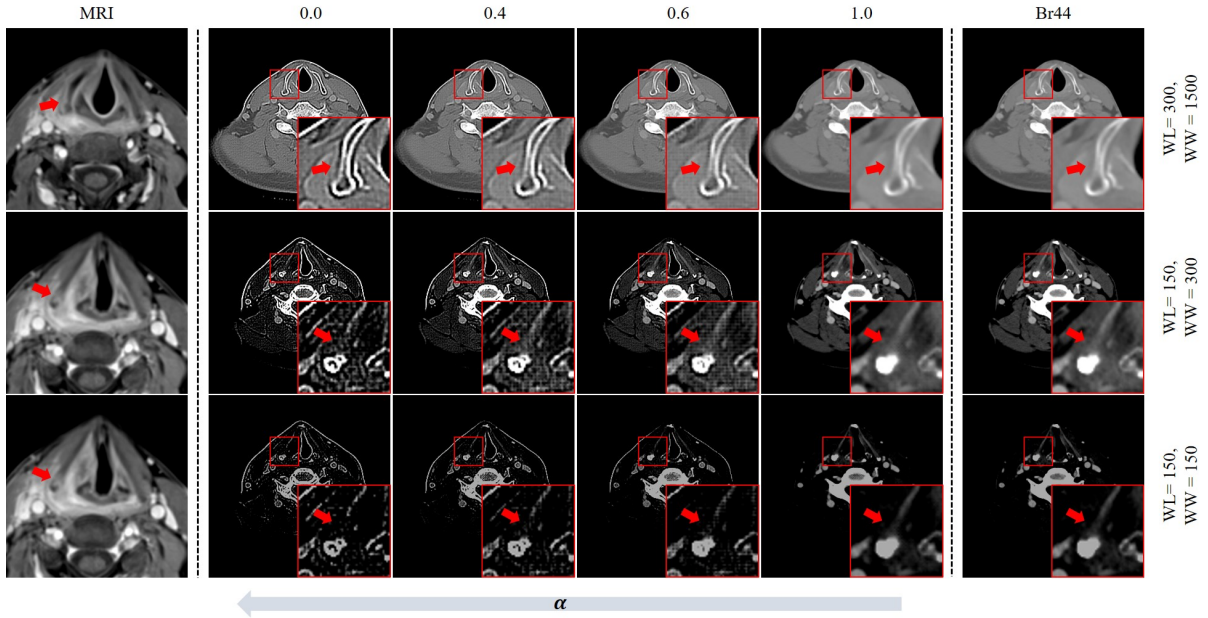


Fig. 8: Cartilage abnormality is clearly seen as  $\alpha$  value varies. The left most column is MR images with contrast enhancement. Right thyroid cartilage tumor infiltration can be observed from MR images whereas it is hard to detect on CT images which are on the right most column. They were reconstructed with Br44 kernel which has similar property as S kernel. The images in the middle were generated from the images in the right most column. Compared to MR images, the generated CT images showed a comparable level of diagnostic ability to check cartilage abnormality.

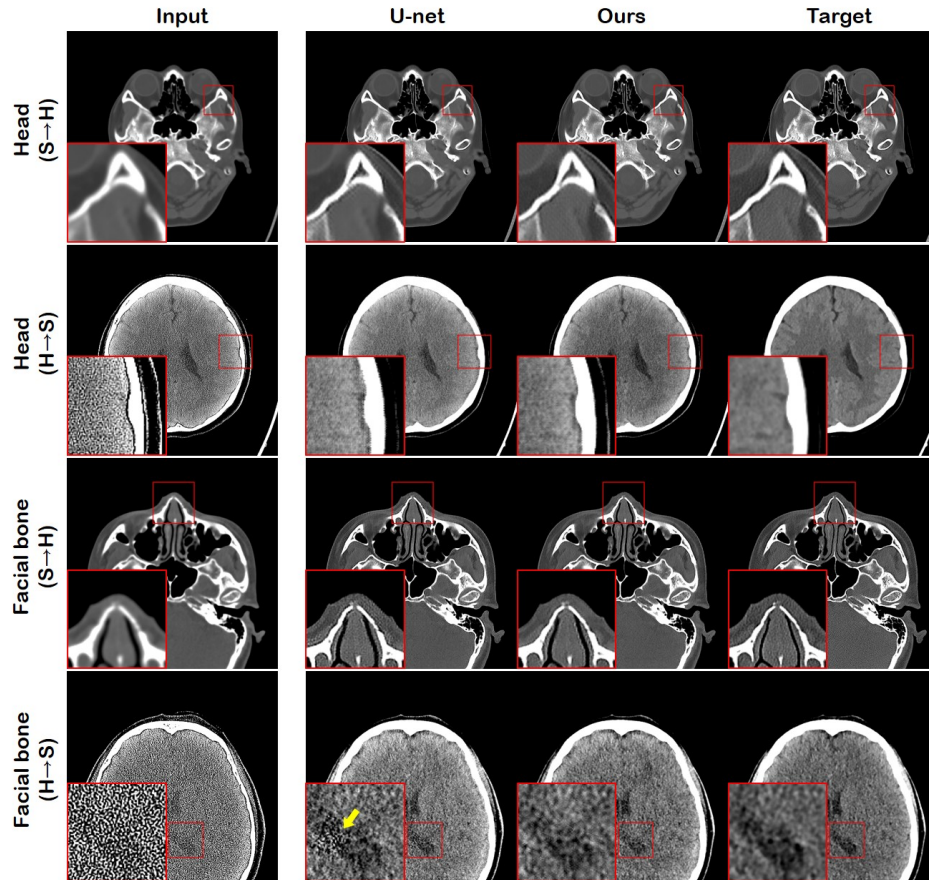


Fig. 9: Comparison between U-Net [16] and Polyphase U-Net.

captured in the generated images if the generators are good enough to approximate both S and H kernel distributions. We could clearly see the shape of the broken bone in the outputs of the Polyphase U-Net. However, as shown in the first and the third row of Figure 9, some irrelevant patterns around bones appeared in the results of the conventional U-Net [16]. These artifacts, on the other hand, did not occur in the generated images of Polyphase U-Net. Thus, we could recognize the stability of the Polyphase U-Net.

Although the similarity in generating S kernel images were not as clear as generating H kernel images, Polyphase U-Net generated slightly better results than the conventional U-Net. As shown in the fourth row of Figure 9, texture of the U-Net-generated images, which should have been as smooth as the target image, is noisy. The improved performance of the Polyphase U-Net was also reflected in the quantitative results (Table II). Since the problem of information loss during pooling operation was resolved in the Polyphase U-Net, it showed better performance compared to the original U-Net.

TABLE II: Quantitative Comparison between U-Net and PolyPhase U-Net

Head	PSNR		SSIM	
	H	S	H	S
CycleGAN with U-Net	31.2706	23.2257	0.8887	0.8615
CycleGAN with PolyPhase U-Net	<b>31.6671</b>	<b>23.9193</b>	<b>0.8922</b>	<b>0.8766</b>

Facial Bone	PSNR		SSIM	
	H	S	H	S
CycleGAN with U-Net	26.1938	18.7120	0.7490	0.7912
CycleGAN with PolyPhase U-Net	<b>26.6328</b>	<b>19.5712</b>	<b>0.7563</b>	<b>0.8336</b>

## VII. CONCLUSION

Different properties of two kernels, H and S kernel, generate two types of reconstructed images. Here, we proposed a post-hoc image domain translation between these two kernels in order to generate one kernel image from the other one. Our proposed method was based on switchable cycleGAN combined with adaptive instance normalization. In addition, thanks to AdaIN, the conversion of kernels could be done with single generator, and various images were generated along the optimal transport path by synergistically combining the two given kernels. The improved performance of our proposed model was proved with extensive experimental results.

## REFERENCES

- [1] P. A. Setiyono, D. Rochmayanti, A. Nino Kurniawan, A. Nugroho Setiawan *et al.*, "The optimization of mastoid CT image using windows and kernel reconstructions," *JPhCS*, vol. 1471, no. 1, p. 012015, 2020.
- [2] K. L. Boedeker, M. F. McNitt-Gray, S. R. Rogers, D. A. Truong, M. S. Brown, D. W. Gjertson, and J. G. Goldin, "Emphysema: effect of reconstruction algorithm on CT imaging measures," *Radiology*, vol. 232, no. 1, pp. 295–301, 2004.
- [3] K. L. Weiss, R. S. Cornelius, A. L. Greeley, D. Sun, I.-Y. J. Chang, W. O. Boyce, and J. L. Weiss, "Hybrid convolution kernel: optimized CT of the head, neck, and spine," *American Journal of Roentgenology*, vol. 196, no. 2, pp. 403–406, 2011.
- [4] S. Takagi, H. Nagase, T. Hayashi, T. Kita, K. Hayashi, S. Sanada, and M. Koike, "Combined multi-kernel head computed tomography images optimized for depicting both brain parenchyma and bone," *Journal of X-Ray Science and Technology*, vol. 22, no. 3, pp. 369–376, 2014.
- [5] S. M. Lee, J.-G. Lee, G. Lee, J. Choe, K.-H. Do, N. Kim, and J. B. Seo, "CT image conversion among different reconstruction kernels without a sinogram by using a convolutional neural network," *Korean journal of radiology*, vol. 20, no. 2, pp. 295–303, 2019.
- [6] J.-Y. Zhu, T. Park, P. Isola, and A. A. Efros, "Unpaired image-to-image translation using cycle-consistent adversarial networks," in *Proceedings of the IEEE international conference on computer vision*, 2017, pp. 2223–2232.
- [7] B. Sim, G. Oh, K. Jeongsol, J. Chanyong, and J. C. Ye, "Optimal transport driven cyclegan for unsupervised learning in inverse problems," *SIAM Jour. Imaging Sciences (to appear)*, Also available as *arXiv preprint arXiv:1909.12116*, 2020.
- [8] C. Villani, *Optimal transport: old and new*. Springer Science & Business Media, 2008, vol. 338.
- [9] G. Peyré, M. Cuturi *et al.*, "Computational optimal transport," *Foundations and Trends in Machine Learning*, vol. 11, no. 5-6, pp. 355–607, 2019.
- [10] X. Huang and S. Belongie, "Arbitrary style transfer in real-time with adaptive instance normalization," in *Proceedings of the IEEE International Conference on Computer Vision*, 2017, pp. 1501–1510.
- [11] J. Gu and J. C. Ye, "Adain-switchable cyclegan for efficient unsupervised low-dose CT denoising," *arXiv preprint arXiv:2008.05753*, 2020.
- [12] A. D. Missert, L. Yu, S. Leng, J. G. Fletcher, and C. H. McCollough, "Synthesizing images from multiple kernels using a deep convolutional neural network," *Medical physics*, vol. 47, no. 2, pp. 422–430, 2020.
- [13] J. Choe, S. M. Lee, K.-H. Do, G. Lee, J.-G. Lee, S. M. Lee, and J. B. Seo, "Deep learning-based image conversion of CT reconstruction kernels improves radiomics reproducibility for pulmonary nodules or masses," *Radiology*, vol. 292, no. 2, pp. 365–373, 2019.
- [14] L. A. Gatys, A. S. Ecker, and M. Bethge, "Image style transfer using convolutional neural networks," in *Proceedings of the IEEE conference on computer vision and pattern recognition*, 2016, pp. 2414–2423.
- [15] Y. Mroueh, "Wasserstein style transfer," *arXiv preprint arXiv:1905.12828*, 2019.
- [16] O. Ronneberger, P. Fischer, and T. Brox, "U-net: Convolutional networks for biomedical image segmentation," in *International Conference on Medical image computing and computer-assisted intervention*. Springer, 2015, pp. 234–241.
- [17] B. Kim and J. C. Ye, "Mumford-shah loss functional for image segmentation with deep learning," *IEEE Transactions on Image Processing*, vol. 29, pp. 1856–1866, 2019.
- [18] X. Mao, Q. Li, H. Xie, R. Y. Lau, Z. Wang, and S. Paul Smolley, "Least squares generative adversarial networks," in *Proceedings of the IEEE International Conference on Computer Vision*, 2017, pp. 2794–2802.
- [19] P. Isola, J.-Y. Zhu, T. Zhou, and A. A. Efros, "Image-to-image translation with conditional adversarial networks," in *Proceedings of the IEEE conference on computer vision and pattern recognition*, 2017, pp. 1125–1134.
- [20] Y. Oh, S. Park, and J. C. Ye, "Deep learning COVID-19 features on CXR using limited training data sets," *IEEE Transactions on Medical Imaging*, vol. 39, no. 8, pp. 2688–2700, 2020.
- [21] D. P. Kingma and J. Ba, "Adam: A method for stochastic optimization," *arXiv preprint arXiv:1412.6980*, 2014.
- [22] A. Paszke, S. Gross, S. Chintala, G. Chanan, E. Yang, Z. DeVito, Z. Lin, A. Desmaison, L. Antiga, and A. Lerer, "Automatic differentiation in pytorch," 2017.
- [23] L. Gallardo-Estrella, D. A. Lynch, M. Prokop, D. Stinson, J. Zach, P. F. Judy, B. van Ginneken, and E. M. van Rikxoort, "Normalizing computed tomography data reconstructed with different filter kernels: effect on emphysema quantification," *European radiology*, vol. 26, no. 2, pp. 478–486, 2016.
- [24] Z. Al-Ameen, G. Sulong, M. Gapar, and M. Johar, "Reducing the gaussian blur artifact from CT medical images by employing a combination of sharpening filters and iterative deblurring algorithms," *Journal of Theoretical and Applied Information Technology*, vol. 46, no. 1, pp. 31–36, 2012.
- [25] Z. Wang, A. C. Bovik, H. R. Sheikh, and E. P. Simoncelli, "Image quality assessment: from error visibility to structural similarity," *IEEE transactions on image processing*, vol. 13, no. 4, pp. 600–612, 2004.